

Simulation of targeted magnetic drug delivery: Two-way coupled biomagnetic fluid dynamics approach

Cite as: Phys. Fluids **34**, 021911 (2022); <https://doi.org/10.1063/5.0080216>

Submitted: 30 November 2021 • Accepted: 27 January 2022 • Published Online: 22 February 2022

Aaiza Gul, Efstratios E. Tzirtzilakis and  Stanislav S. Makhanov

COLLECTIONS

 This paper was selected as Featured

 This paper was selected as Scilight



View Online



Export Citation



CrossMark

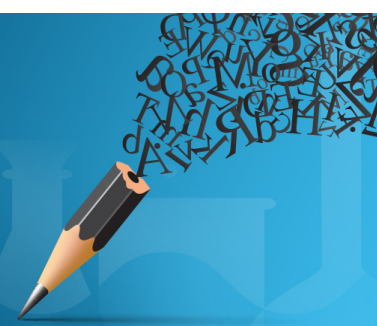


Author Services

English Language Editing

High-quality assistance from subject specialists

LEARN MORE



Simulation of targeted magnetic drug delivery: Two-way coupled biomagnetic fluid dynamics approach

Cite as: Phys. Fluids **34**, 021911 (2022); doi: 10.1063/5.0080216

Submitted: 30 November 2021 · Accepted: 27 January 2022 ·

Published Online: 22 February 2022



View Online



Export Citation



CrossMark

Aaiza Gul,¹ Efstratios E. Tzirtzilakis,² and Stanislav S. Makhanov^{1,a)} 

AFFILIATIONS

¹School of Information, Computer, and Communication Technology, Sirindhorn International Institute of Technology Bangkadi Campus, Thammasat University, 200 Moo 5, Tiwanon Rd. Bangkadi, Mueang Pathumthani 12000, Thailand

²Fluid Mechanics and Turbomachinery Laboratory, Department of Mechanical Engineering, University of the Peloponnese, 1M Aleksandrou Str., Koukoulis 263 34 Patras, Greece

^{a)}Author to whom correspondence should be addressed: makhanov@siit.tu.ac.th

ABSTRACT

Due to significant advances in nanomedicine, magnetic nanoparticles (MNs) have emerged as a promising carrier in targeted magnetic drug delivery (TMDD) systems. Therefore, this paper presents a computational model for optimized magnetic navigation of MNs coated with the anticancer drugs inside the blood vessels. A mixture of blood and MNs is represented as a one-phase solution in the majority of TMDD models. The preceding two-phase models are usually one-way coupled, i.e., the blood flow has a significant influence on the MNs flow. However, the inverse effect of the MNs on the blood flow is not taken into account. To overcome these limitations, the MNs in a blood vessel are simulated by a two-phase (solid–liquid) flow governed by two-way coupled momentum and temperature equations for the blood flow and the MNs. The numerical procedure invokes the stream function–vorticity formulation and an efficient numerical method on a finite-difference grid. The model, validated by the experimental results, has been applied to analyze the formation of vortices relative to the magnetic force and the drag force and the zones of TMDD, where the velocity of the blood flow is low and the velocity of the MNs is high toward the magnet. The model has been verified against the existing models and the experimental data. The numerical results show that the magnetohydrodynamics slows down the blood flow and smooths vortices created by Ferrohydrodynamics. The size of the drug-loaded MNs on the velocity and the temperature of the blood has been evaluated.

Published under an exclusive license by AIP Publishing. <https://doi.org/10.1063/5.0080216>

I. INTRODUCTION

Despite advances in cancer treatment over the previous four decades, cancer detection and treatment continue to be a global healthcare concern.^{1–4} Furthermore, magnetic nanoparticles' (MNs) carriers with suitable dimensions can provide the best solutions for medical drugs preparations.⁵ The most effective anti-cancer medications are doxorubicin drugs. The usage of these medications results in the death of healthy cells as well. Widder *et al.*⁶ conducted an experimental study of Yoshida sarcoma tumors in rats. They found that high doses of doxorubicin (0.5–5 mg/kg) had a harmful effect with an average weight loss of 12 g in rats given large doses, indicating systemic toxicity. Animals treated with low doses of doxorubicin gained 23.3 and 17.8 g of weight.

An electrocardiogram records the electrical activity of the heart; however, it has been discovered that when the electrocardiogram was

utilized for gating during MRI, the signal was distorted.⁷ The explanation is based on the Magnetohydrodynamics (MHD) effects, which state that when the blood flows through the magnetic field (MF), it generates voltages that superimpose the electrocardiogram.⁸ The plasma ions in blood generate an electric current that interacts with the MF. The Lorentz force is produced as a result of this interaction. Later on, many studies have been conducted to analyze the effects of the MF on cardiovascular system and microcirculation.^{9–15}

The general analysis of the effects of the MF is a subject of Biomagnetic Fluid Dynamics (BFD) that incorporates the principles of both MHD and Ferrohydrodynamics (FHD). In 2004–2005, Loukopoulos and Tzirtzilakis¹⁶ and Tzirtzilakis and Loukopoulos¹⁷ developed a combined FHD/MHD steady state finite-difference numerical model with an external MF. Tzirtzilakis¹⁸ reported a 3D BFD model, considering FHD and MHD in a rectangular duct.

The FHD model implies that the fluids subjected to an external MF exhibit magnetization, whereas the MHD model is of an electrically conducting fluid under the impact of the Lorentz force. The FHD is essential for the formation of vortices, while the Lorentz force may reduce the blood flow and smooth vortices.^{19,20}

The most important part of the design and mathematical modeling of TMDD is to get insights into the behavior of the MN–blood flow when a strong non-uniform MF exists.^{21–23} Therefore, it is important to consider the combined effects of MHD and FHD.

In the present study, we offer the BFD¹⁸ that incorporates the principles of both the FHD and MHD along with a two-phase two-way coupled model.²³ The approach enables us to examine the effect of both MHD and FHD as well as the individual effect of either MHD or FHD. Note that the standard two-phase model is based on combining the hydrodynamic and magnetic forces. However, the corresponding continuity, momentum, and energy equations of the solid phase are not included. In contrast, the proposed model includes the drug-loaded MNs having a two-way momentum exchange. The model includes the reverse impact of the MNs on the blood flow. In particular, it is possible to analyze the impact of the size and the concentration of the MNs on the blood flow. It has been shown that under certain conditions, the geometric structure of the MNs' flow is drastically different from that of the blood flow. The formation, velocity, size, and geometry of the vortices that appear in the blood flow can be evaluated. The model has been analyzed with reference to single-phase models^{24,25} and a two-phase model.²³ Furthermore, numerical experiments are presented for the two-dimensional coupled blood-MNs' flow in a rectangular channel. The model makes it possible to analyze the impact of the Lorentz force (MHD). Furthermore, the numerical analysis of the flow patterns relative to the size of the MNs and the concentration of the drug within the MNs is presented. Finally, it has been demonstrated that the size of the drug-loaded MNs has an impact on the temperature of the blood. Under certain conditions, the MF acting on drug-loaded MNs increases the blood temperature. Simulation of the above-mentioned effects is possible only with the proposed two-way coupled, two-phase model and its possible extensions.

II. MATHEMATICAL FORMULATION

Consider a viscous, unsteady, two-phase flow consisting of the MNs and the blood in a two-dimensional rectangular channel with

length L and height h (Fig. 1). The flow is assumed to be electrically conducting as well as magnetized. The upper and lower walls have a constant temperature. The magnetic source is a wire placed perpendicular to the (x,y) -plane at the point (a,b) below the lower wall. The governing equations of the two-phase, two-way coupled flow are given with regard to velocity $\mathbf{V} = (u, v)$ and temperature T of the blood and the particles¹⁸ (the subscript p indicates the parameters of the MNs flow).

$$\nabla \cdot \mathbf{V} = 0, \tag{1}$$

$$\rho \left(\frac{\partial u}{\partial t} + \mathbf{V} \cdot \nabla \mathbf{V} \right) = -\nabla p + \mu \nabla^2 \mathbf{V} + \mathbf{F} + \mu_0 M \nabla H - \sigma B^2 \mathbf{V}, \tag{2}$$

$$\rho c \left(\frac{\partial T}{\partial t} + \mathbf{V} \cdot \nabla T \right) + \mu_0 T \frac{\partial M}{\partial T} \mathbf{V} \cdot \nabla H - \sigma B^2 \mathbf{V}^2 = k \nabla^2 T + Q_p, \tag{3}$$

where the drag force \mathbf{F} is given by

$$\mathbf{F} = C_v \rho_p F_D (\mathbf{V}_p - \mathbf{V}), \tag{4}$$

and

$$Q_p = C_v \rho_p c_p h_v (T_p - T). \tag{5}$$

The electric conductivity of MNs (Fe_3O_4) is determined by the temperature of the surrounding environment. It is a conductor at room temperature, but it is an insulator at temperatures below 120 K (-153.15°C).^{26,27} Thus, the solid phase equations are given by

$$\nabla \cdot \mathbf{V}_p = 0, \tag{6}$$

$$\rho_p C_v \left(\frac{\partial \mathbf{V}_p}{\partial t} + \mathbf{V}_p \cdot \nabla \mathbf{V}_p \right) = -(1 - C_v) \mathbf{F} + C_v \mu_0 M \nabla H - C_v \sigma_p B^2 \mathbf{V}_p, \tag{7}$$

$$\begin{aligned} \rho_p c_p C_v \left(\frac{\partial T_p}{\partial t} + \mathbf{V}_p \cdot \nabla T_p \right) + C_v \mu_0 T_p \frac{\partial M}{\partial T_p} \mathbf{V}_p \cdot \nabla H - \sigma B^2 \mathbf{V}_p^2 \\ = -(1 - C_v) Q_p, \end{aligned} \tag{8}$$

where p is the pressure, ρ is the density, μ is the dynamic viscosity, c is the heat capacity, k is the thermal conductivity, C_v is the concentration of MNs in the blood, σ is the electrical conductivity, and $\mu_0 = 4\pi \times 10^{-7} \text{ Hm}^{-1}$ is the magnetic permeability of vacuum.²⁸ Note that

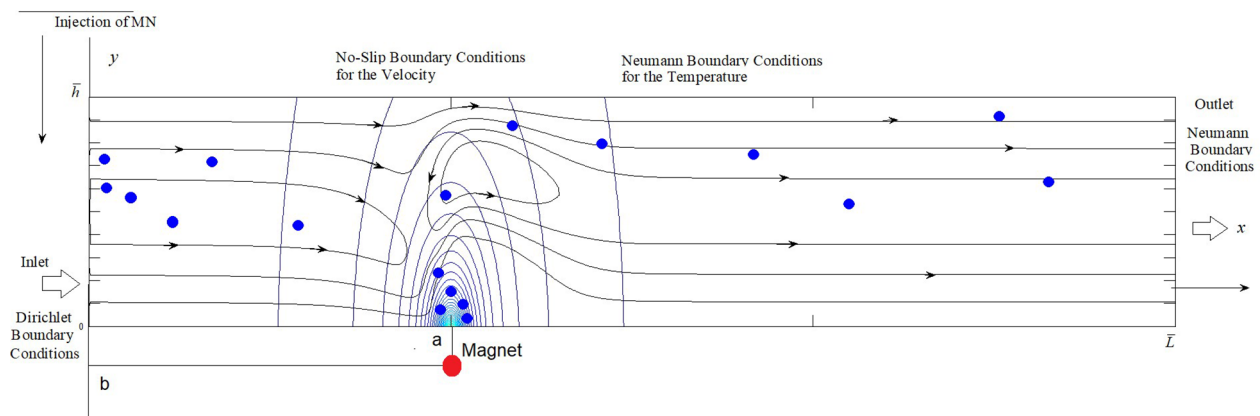


FIG. 1. Flow domain and boundary conditions.

Eq. (7) is derived under the assumption of the low magnetic Reynolds number defined as the ratio of advection to diffusion of the MF.

The additional term $\mu_0 M \nabla H$ in the momentum Eq. (2) is the MF per unit volume, whereas $\mu_0 T_p \frac{\partial M}{\partial T_p} \mathbf{V}_p \nabla H$ in Eq. (8) is the thermal power per unit volume due to the magnetocaloric effect. Finally, Eqs. (1)–(7) treat the phases as a continuum. Each phase is characterized by an individual continuity, momentum, and energy equation. The phases interact with each other through Eqs. (4) and (5).

A. Magnetic field and magnetization

Following Tzirtzilakis,^{24,29} consider a magnetic source (a current-carrying wire conductor) positioned perpendicular to the (x, y) plane. H denotes the intensity of the MF given by

$$H = \sqrt{H_x^2 + H_y^2}. \quad (9)$$

The magnetization M is approximated by³⁰

$$M = KH(T_c - T), \quad (10)$$

where K is an experimental constant and T_c is the Curie temperature. Following Tzirtzilakis,^{24,25} we consider a magnetic source (a current-carrying wire conductor) positioned perpendicular to the (x, y) plane. The wire is at the position (a, b) below the lower wall (Fig. 1). The strength of the MF is defined by the magnetic induction given by $B(x, y) = \mu_0 \mathbf{H} \equiv \mu_0 (H_x, H_y)$,¹⁸ where

$$H_x = \frac{\gamma}{2\pi} \frac{(y-b)}{(x-a)^2 + (y-b)^2}, \quad H_y = -\frac{\gamma}{2\pi} \frac{(x-a)}{(x-a)^2 + (y-b)^2}, \quad (11)$$

where γ is the intensity of the MF at the source.

B. Drug concentration

The density of the MNs containing a magnetic core is given by

$$\rho_p = \rho_{core} d_{mp}^3 + \rho_{shell} (1 - d_{mp}^3), \quad (12a)$$

where d_{mp} is the ratio of magnetic-core d_m and diameter d of the MNs. For $d_{mp} = 1$, we have fully magnetic particles, whereas for $d_{mp} = 0$, they become magnetically neutral. In this study, $d_{mp} = 0.84$.⁵ The shell is a mixture of a therapeutic drug and a carrier. The shell density is given by⁵

$$\rho_{shell} = \left(\frac{f_1}{\rho_{drug}} + \frac{1-f_1}{\rho_{carrier}} \right)^{-1}, \quad (12b)$$

where f_1 is the fractional loading of the drug within the shell. In the present work, the magnetic core is made from the ferromagnetic nanoparticles Fe_3O_4 with the density of $\rho_{core} = 5200 \text{ kg/m}^3$, magnetic susceptibility $\chi_2 = 20$, and saturation magnetization $M_{sat} = 448 \text{ kA/m}$. The shell carrier is biodegradable poly(lactide-co-glycolide) (PLGA) or poly(ethylene) glycol (PEG) with the density $\rho_{carrier} = 1300 \text{ kg/m}^3$ and $\rho_{carrier} = 1126 \text{ kg/m}^3$, respectively. Unless stated otherwise, the fractional loading of the drug is taken to be $f_1 = 30\%$. Their typical density $\rho_{drug} = 1610 \text{ kg/m}^3$, which corresponds to some anti-cancer drugs.

C. Drag and heat transfer coefficients

Following Bianco *et al.*,²⁵ Stokes' resistance law for small Re_p and sub-micrometer particles is given by

$$F_D \approx f \frac{1}{\tau_p} = \frac{18\mu}{d^2 \rho_p C_c}, \quad (13)$$

where d is the diameter of the particle, f is the drag coefficient, and τ_p is the particle response time. The Cunningham correction coefficient is given by

$$C_c = 1 + \frac{2\lambda_a}{d} (1.257 + 0.4e^{-\frac{1.1d}{\lambda_a}}), \quad (14)$$

where λ_a is the mean free path of the nanoparticle.

Furthermore,

$$\text{Re}_p = \frac{d\rho}{\mu} \tilde{u}_0, \quad (15)$$

where \tilde{u}_0 denotes the average and index 0 refers to the inlet boundary.

The drag coefficient is defined by

$$f = \begin{cases} 1, & \text{if } \text{Re}_p \leq 1, \\ \text{Re}_p^{0.354}, & \text{if } 1 < \text{Re}_p < 400. \end{cases} \quad (16)$$

The energy equation for spherical MNs is given by $h_v = \frac{6h_h}{d}$, where h_h is the heat coefficient at the blood/MNs interface.³¹ The Nusselt number Nu_p is given by³¹

$$\text{Nu}_p \equiv \frac{h_h d}{k} = 2.0 + 0.6 \text{Re}_p^{1/2} \text{Pr}^{1/3}. \quad (17)$$

Hence, $h_h = \frac{k}{d} (2.0 + 0.6 \text{Re}_p^{1/2} \text{Pr}^{1/3})$.

D. Boundary conditions

We assume a parabolic profile of the velocity and constant temperature of the fluid and the particles at the inlet. At the outflow, a fully developed flow is considered, i.e., the axial derivative $\frac{\partial}{\partial y}$ of all quantities is considered to be zero. At the walls, we adopt the no-slip conditions for the fluid and the particles. The walls are thermally insulated. Hence, the boundary conditions are

$$\begin{aligned} \text{Inflow: } x = 0, 0 \leq y \leq h: & \quad u = u_p = u_0(y), \\ & \quad v = v_p = 0; \quad T = T_p = 37^\circ\text{C}. \end{aligned} \quad (18)$$

$$\begin{aligned} \text{Outflow: } x = L, 0 \leq y \leq h: & \quad \frac{\partial \Omega}{\partial x} = 0, \quad \Omega = u, v, T, u_p, v_p, T_p. \end{aligned} \quad (19)$$

$$\begin{aligned} \text{Upper boundary: } y = h, 0 \leq x \leq L: & \quad u = u_p = 0; \\ & \quad v = v_p = 0; \quad \frac{\partial T_w}{\partial y} = \frac{\partial T_p}{\partial y} = 0. \end{aligned} \quad (20)$$

$$\begin{aligned} \text{Lower boundary: } y = 0, 0 \leq x \leq L: & \quad u = u_p = 0; \\ & \quad v = v_p = 0, \quad \frac{\partial T_w}{\partial y} = \frac{\partial T_p}{\partial y} = 0. \end{aligned} \quad (21)$$

$$\begin{aligned} \text{Initial conditions: } 0 \leq x \leq L, 0 \leq y \leq h: & \quad u = v = 0; \\ & \quad u_p = v_p = 0; \quad T = T_p = 37^\circ\text{C}. \end{aligned} \quad (22)$$

Note that the no-slip conditions imply that the particles may adhere on the wall, thus altering the geometry of the boundary. Moreover, since Equations (1)–(7) do not include the concentration of MNs there is no way to obtain the possible changes at the wall. The assumption is that most of the particles bounce-up from the boundary. Therefore, the geometry of the wall does not change. However, this assumption

may not be correct for large nanoparticles. The two-phase flow for the large particles formulated as a problem with a moving boundary requires much experimental data and detailed observations. Nevertheless, for these dimensions, the proposed boundary conditions are plausible.

III. DIMENSIONLESS EQUATIONS

The following dimensionless variables are introduced:

$$\begin{aligned} \bar{u} &= \frac{u}{u_r}, \quad \bar{v} = \frac{v}{u_r}, \quad \bar{\xi} = \frac{x}{h}, \quad \bar{\eta} = \frac{y}{h}, \quad \bar{t} = \frac{t\mu}{\rho h^2}, \\ \bar{t}_1 &= \frac{t_1\mu}{\rho d^2}, \quad \bar{p} = \frac{p}{\rho u_r^2}, \quad \bar{u}_p = \frac{u_p}{u_{r1}}, \quad \bar{v}_p = \frac{v_p}{u_{r1}}, \\ \bar{H} &= \frac{H}{\gamma}, \quad \bar{T}_p = (T_p - T_0) \frac{k}{qh}, \quad \bar{T} = (T - T_0) \frac{k}{qh}, \end{aligned} \quad (23)$$

where T_0 is the temperature of the MNs at the channel inlet and q is the heat flux. All other notations are self-explanatory and identical to the notations in Eqs. (1)–(8). However, the new variables are dimensionless. Furthermore, we omit the overbars for the new dimensionless variables.

Let us introduce the vorticity function $J(\xi, \eta)$ and the stream function $\psi(\xi, \eta)$ as follows:

$$\begin{aligned} J(\xi, \eta) &= \frac{\partial v}{\partial \xi} - \frac{\partial u}{\partial \eta}, \quad J_p(\xi, \eta) = \frac{\partial v_p}{\partial \xi} - \frac{\partial u_p}{\partial \eta}, \quad u = \frac{\partial \psi}{\partial \eta}, \\ u_p &= \frac{\partial \psi_p}{\partial \eta}, \quad v = -\frac{\partial \psi}{\partial \xi}, \quad v_p = -\frac{\partial \psi_p}{\partial \xi}. \end{aligned} \quad (24)$$

The pressure is eliminated from Eq. (2). Substituting Eq. (24) into Eqs. (1)–(3) and (6)–(8) yields

$$\frac{\partial^2 \psi}{\partial \xi^2} + \frac{\partial^2 \psi}{\partial \eta^2} = -J, \quad \frac{\partial^2 \psi_p}{\partial \xi^2} + \frac{\partial^2 \psi_p}{\partial \eta^2} = -J_p, \quad (25)$$

$$\begin{aligned} \frac{\partial J}{\partial t} &= \frac{\partial^2 J}{\partial \xi^2} + \frac{\partial^2 J}{\partial \eta^2} - \text{Re} \left(\frac{\partial J}{\partial \xi} \frac{\partial \psi}{\partial \eta} - \frac{\partial J}{\partial \eta} \frac{\partial \psi}{\partial \xi} \right) + C_v \beta_1 D_p \text{Re} (U_2 J_p - U_2^2 J) \\ &+ M_{\text{nF}} \text{Re} H \left(\frac{\partial H}{\partial \xi} \frac{\partial T}{\partial \eta} - \frac{\partial H}{\partial \eta} \frac{\partial T}{\partial \xi} \right) + M_{\text{nM}} H^2 \left(\frac{\partial^2 \psi}{\partial \eta^2} \right), \end{aligned} \quad (26a)$$

$$\begin{aligned} \frac{\partial J_p}{\partial t} &= \text{Re}_p d_o \left(- \left(\frac{\partial J_p}{\partial \xi} \frac{\partial \psi_p}{\partial \eta} - \frac{\partial J_p}{\partial \eta} \frac{\partial \psi_p}{\partial \xi} \right) - (1 - C_v) \beta_1 (U_2 J_p - U_2^2 J) \right) \\ &+ M_{\text{nF}_p} H \left(\frac{\partial H}{\partial \xi} \frac{\partial T_p}{\partial \eta} - \frac{\partial H}{\partial \eta} \frac{\partial T_p}{\partial \xi} \right) + M_{\text{nM}_p} H^2 \left(\frac{\partial^2 \psi_p}{\partial \eta^2} \right), \end{aligned} \quad (26b)$$

$$\begin{aligned} \text{Pr} \frac{\partial T}{\partial t} &= \frac{\partial^2 T}{\partial \xi^2} + \frac{\partial^2 T}{\partial \eta^2} - \text{Pr} \text{Re} \left(\frac{\partial T}{\partial \xi} \frac{\partial \psi}{\partial \eta} - \frac{\partial T}{\partial \eta} \frac{\partial \psi}{\partial \xi} \right) \\ &+ \text{Pr} \text{Re} C_v D_p \gamma_p \beta_2 (u_{r2} T_p - u_{r2}^2 T) M_{\text{nM}} \text{Pr} \text{Ec} H^2 \left(\frac{\partial \psi}{\partial \eta} \right)^2 \\ &+ M_{\text{nF}} \text{Pr} \text{Re} \text{Ec} H T_p \left(\frac{\partial H}{\partial \xi} \frac{\partial T_p}{\partial \eta} - \frac{\partial H}{\partial \eta} \frac{\partial T_p}{\partial \xi} \right) \\ &+ \text{Pr} \text{Re} \left\{ \left(\frac{\partial^2 \psi}{\partial \eta^2} - \frac{\partial^2 \psi}{\partial \xi^2} \right)^2 + 4 \left(\frac{\partial^2 \psi}{\partial \xi \partial \eta} \right)^2 \right\}, \end{aligned} \quad (26c)$$

$$\begin{aligned} \frac{\partial T_p}{\partial t} &= - \text{Re}_p d_o \left(\frac{\partial T_p}{\partial \xi} \frac{\partial \psi_p}{\partial \eta} - \frac{\partial T_p}{\partial \eta} \frac{\partial \psi_p}{\partial \xi} \right) - (1 - C_v) \text{Re}_p d_o \beta_2 (T_p - T) \\ &+ \frac{\text{Re}_p d_o M_{\text{nF}_p} \text{Ec}}{\gamma_1 U_2^2} H^2 \left(\frac{\partial \psi_p}{\partial \eta} \right)^2 + \frac{\text{Re}_p d_o M_{\text{nF}_p} \text{Ec}}{\gamma_1 U_2^2} \\ &\times H T_p \left(\frac{\partial H}{\partial \xi} \frac{\partial \psi_p}{\partial \eta} - \frac{\partial H}{\partial \eta} \frac{\partial \psi_p}{\partial \xi} \right). \end{aligned} \quad (27a)$$

The additional non-dimensional parameters are as follows:

$$\begin{aligned} M_{\text{nF}} &= \frac{\mu_0 K H_0^2 k}{\rho u_r^2 q_0 h}, \quad M_{\text{nF}_p} = \frac{\mu_0 K H_0^2 k}{\rho_p u_{r1}^2 q_0 h}, \quad M_{\text{nM}} = \frac{\mu_0^2 H_0^2 h^2 \sigma}{\mu}, \\ M_{\text{nM}_p} &= \frac{\mu_0^2 H_0^2 d^2 \sigma_p}{\mu}, \quad \beta_1 = \frac{1}{\text{St}} = F_D \frac{h}{u_r}, \quad \beta_2 = \frac{6 h_v h}{d u_r}, \\ U_2 &= \frac{u_r}{u_{r1}}, \quad \gamma_1 = \frac{c_p}{c}, \quad d_o = \frac{d}{h}, \quad D_p = \frac{\rho_p}{\rho}, \end{aligned}$$

where M_{nF} , M_{nF_p} , M_{nM} , and M_{nM_p} are the magnetic numbers corresponding to FHD and MHD of the blood and MNs. β_1 , β_2 control the energy transfer between the blood flow and MNs, and U_2 is the ratio of the maximum velocity of the flow to the maximum velocity of the MNs at the entrance. γ_p , d_o , D_p are the ratios of the heat capacity, size, and density of the MNs to the heat capacity, channel height, and density of the blood, respectively. Re , Ec , and St are the Reynolds number, the Eckert number, the Stokes number, and the Prandtl number, respectively. Finally, the time dependent model makes it possible to evaluate the steady state time t_s . In other words, it is important to evaluate the time required to achieve the regions of the targeted magnetic drug delivery (TMDD), where the velocity of the blood flow is low and the velocity of the MNs is high toward the magnet. Aside from this, even when the steady-state time is not required, the pseudo-time variable makes it possible to arrange iterative numerical solution. Decreasing the time step improves stability of the algorithm.

IV. NUMERICAL METHOD

The equations for the stream functions of the blood and the MNs' flow (25) are approximated by the standard finite-difference equations and solved by the block Gauss-Seidel method.³² This is followed by a correction similar to the successive over-relaxation as follows: $\psi_{\text{new}}^{k+1} = \psi_{\text{GS}}^{k+1} \theta + (1 - \theta) \psi_{\text{GS}}^k$, where ψ_{GS}^{k+1} is the numerical solution obtained by the block Gauss-Seidel method, ψ_{GS}^k is the solution at the previous iteration step k , and θ is the relaxation parameter. Note that Eqs. (25) depend implicitly on time because of J , J_p at the right-hand sides. Hence, the equations must be solved at every time step. The functions J , J_p are taken from the n th time step. The numerical solution of Eqs. (27b)–(29a) is based on a similar procedure, including the block Gauss-Seidel and the successive over-relaxation. Writing (26a)–(27a) in the standard form yields

$$\frac{\partial J}{\partial t} = A_1 \frac{\partial^2 J}{\partial x^2} + B_1 \frac{\partial^2 J}{\partial y^2} + C_1 \frac{\partial J}{\partial x} + D_1 \frac{\partial J}{\partial y} + E_1 J + F_1, \quad (27b)$$

$$\frac{\partial J_p}{\partial t} = C_2 \frac{\partial J_p}{\partial x} + D_2 \frac{\partial J_p}{\partial y} + E_2 J + F_2, \quad (28a)$$

$$\frac{\partial T}{\partial t} = A_3 \frac{\partial^2 T}{\partial x^2} + B_3 \frac{\partial^2 T}{\partial y^2} + C_3 \frac{\partial T}{\partial x} + D_3 \frac{\partial T}{\partial y} + E_3 J + F_3, \quad (28b)$$

$$\frac{\partial T_p}{\partial t} = C_4 \frac{\partial T_p}{\partial x} + D_4 \frac{\partial T_p}{\partial y} + E_4 J + F_4, \tag{29a}$$

where coefficients $A_i, B_i, C_i, D_i,$ and F_i depend on the other unknowns and their partial derivatives. We apply the standard second-order finite-difference approximation to the second derivatives and the upwind first-order approximation to the first derivatives. For instance, (27b) is approximated as follows:

$$\begin{aligned} \frac{J_{ij}^{n+1} - J_{ij}^n}{\tau} = & A_{1,ij}^n \frac{J_{i+1,j}^{n+1} - 2J_{ij}^{n+1} + J_{i-1,j}^{n+1}}{\Delta x^2} + B_{1,ij}^n \frac{J_{i,j+1}^{n+1} - 2J_{ij}^{n+1} + J_{i,j-1}^{n+1}}{\Delta y^2} \\ & + C_{1,ij}^n \frac{J_{i+1,j}^{n+1} - J_{ij}^{n+1}}{\Delta x} + C''_{1,ij} \frac{J_{ij}^{n+1} - J_{i-1,j}^{n+1}}{\Delta x} + D_{1,ij}^n \frac{J_{i,j+1}^{n+1} - J_{ij}^n}{\Delta y} \\ & + D''_{1,ij} \frac{J_{ij}^{n+1} - J_{i,j-1}^{n+1}}{\Delta y} + E_{1,ij} J_{ij}^{n+1} + F(T_{ij}^n, T_{p,ij}^n, \psi^{n+1}, \psi_p^{n+1}), \end{aligned} \tag{29b}$$

where $J_{ij}^n = J_{ij}(x_i, y_j, n\tau)$, τ is the time step, $\Delta x = \frac{1}{N}$, $\Delta y = \frac{1}{M}$ are the spatial steps, $x_i = i\Delta x$, $y_j = j\Delta y$, $i = \overline{1, N-1}$, $j = \overline{1, M-1}$, N is the number of points in the x -direction, M is the number of points in the y -direction, $C' = \frac{C+|C|}{2}$, $C'' = \frac{C-|C|}{2}$, $D' = \frac{D+|D|}{2}$, and $D'' = \frac{D-|D|}{2}$.

For $i = 0, N$ and $j = 0, M$, (29b) is replaced by an approximation of the boundary conditions. The resulting tri-diagonal matrix is inverted by the Thomas algorithm. The first-order upwind differences in (29b) result in the first-order approximation; however, the corresponding matrix is diagonally dominant. Consequently, the Thomas algorithm is stable.³³ The system (27b)–(29a) is solved by the following iterative algorithm:

- (1) Calculate $\psi^{n+1,l+1}$ and $\psi_p^{n+1,l+1}$ by solving (25), where J and J_p are taken from the previous iteration l .
- (2) Substitute $\psi^{n+1,l+1}$, $\psi_p^{n+1,l+1}$ into (25)–(29b). Find $J^{n+1,l+1}$ and $J_p^{n+1,l+1}$, where $T^{n+1,l}$, $T_p^{n+1,l}$ are taken from the previous iteration l .
- (3) Substitute $\psi^{n+1,l+1}$, $\psi_p^{n+1,l+1}$, $J^{n+1,l+1}$, $J_p^{n+1,l+1}$. Find $T^{n+1,l+1}$, $T_p^{n+1,l+1}$.
- (4) The convergence is established when

$$\Delta = \max_{ij,U} |U^{l+1} - U^l| < \varepsilon,$$

where $U = J, J_p, \psi, \psi_p, T, T_p$, and ε is the required accuracy.

- (5) If $\Delta \geq \varepsilon$, return to step 1.

V. RESULTS AND DISCUSSION

Testing hydrodynamic models of the targeted magnetic drug delivery (TMDD) is hampered by lack of the available data. Until now,

the measurements of the velocity of the blood and MNs' flow data inside the vessels during the TMDD are not available. However, there exist a few experimental studies relevant to the temperature of the nanofluids. These measurements are technically feasible and can be accomplished by standard medical equipment. Therefore, the proposed model is validated by (1) comparing with the preceding models and (2) comparing with the measurements of the temperature of the nanofluids. The model is tested against Tzirtzilakis,²⁴ Bianco *et al.*,²⁵ and Boutopoulos *et al.*²³ Experimental data are taken from Wen and Ding.³⁵ The setup of the numerical experiments follows Nacev *et al.*³⁴

A. Validation of the model

We compare the proposed two-phase, two-way model (TPM) with the single-phase model (SPM₁) of Tzirtzilakis,²⁴ the single-phase model of Bianco *et al.*²⁵ (SPM₂) and the double-phase, one-way coupled model (OW) of Boutopoulos *et al.*²³

Consider case 1: $25 \leq Re \leq 500$, $\beta_2 \approx 4$, $St \approx 3.56 \times 10^{-4}$, $C_v = 0.001$, and $d = 250$. Figure 2 displays the streamlines and the density plot of the magnitude of the velocity for the steady-state solution obtained by the SPM₁, OW, and TPM. The solutions are practically identical. The difference between the solutions by the TPM and the reference models does not exceed 10^{-4} .

The above tests are considered as a partial validation of the model. However, for large d , the proposed model shows different results. As an example, consider case 2: $d = 20\,000$ (all other parameters are the same). Note that SPM₁ does not include d . Therefore, we test against the solution similar to that shown in Fig. 2. Figures 3(a)–3(c) show the steady-state solution for SPM₁, OW, and TPM. Clearly, in the case of large d , the results obtained by the proposed model are different since the MNs have a reverse impact on the dynamics of the blood. For instance, the maximum difference between the solution by SPM₁ and TPM is about 0.9 cm/s.

Wen and Ding³⁵ experimentally evaluated the average Nusselt number measuring the convective heat transfer of nanofluids flowing through a copper tube in the laminar flow regime. The copper tube was 970 mm length, 4.5 mm inner diameter, and 6.4 mm outer diameter. Their experimental setup is shown in Fig. 4.

The setup consists of four units: the flow loop, the measuring unit, the heating unit, and the cooling unit. The flow loop further includes four sections: the pump with a built-in flow meter, the test section, the reservoir, and the collection tank. The test section consists of a straight copper tube heated by a silicon rubber flexible heater linked to a DC power supply. The nanofluid flows through the copper tube. Thermocouples are used to measure the temperature at the inlet and outlet flow. The Nusselt number is evaluated by

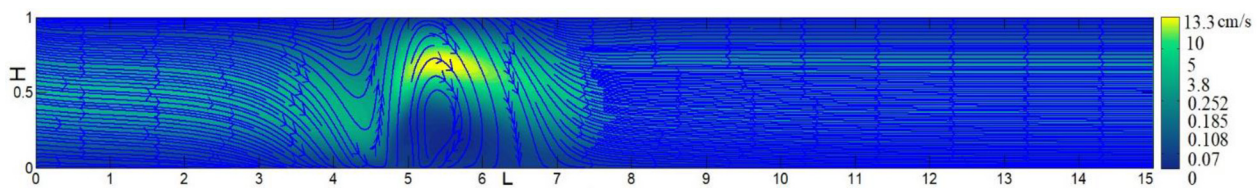


FIG. 2. Blood flow, case 1. The reference models generate similar solutions: $C_v = 0.001$ and $d = 250$. The curves denote the stream lines. The density plot shows the magnitude of the velocity.

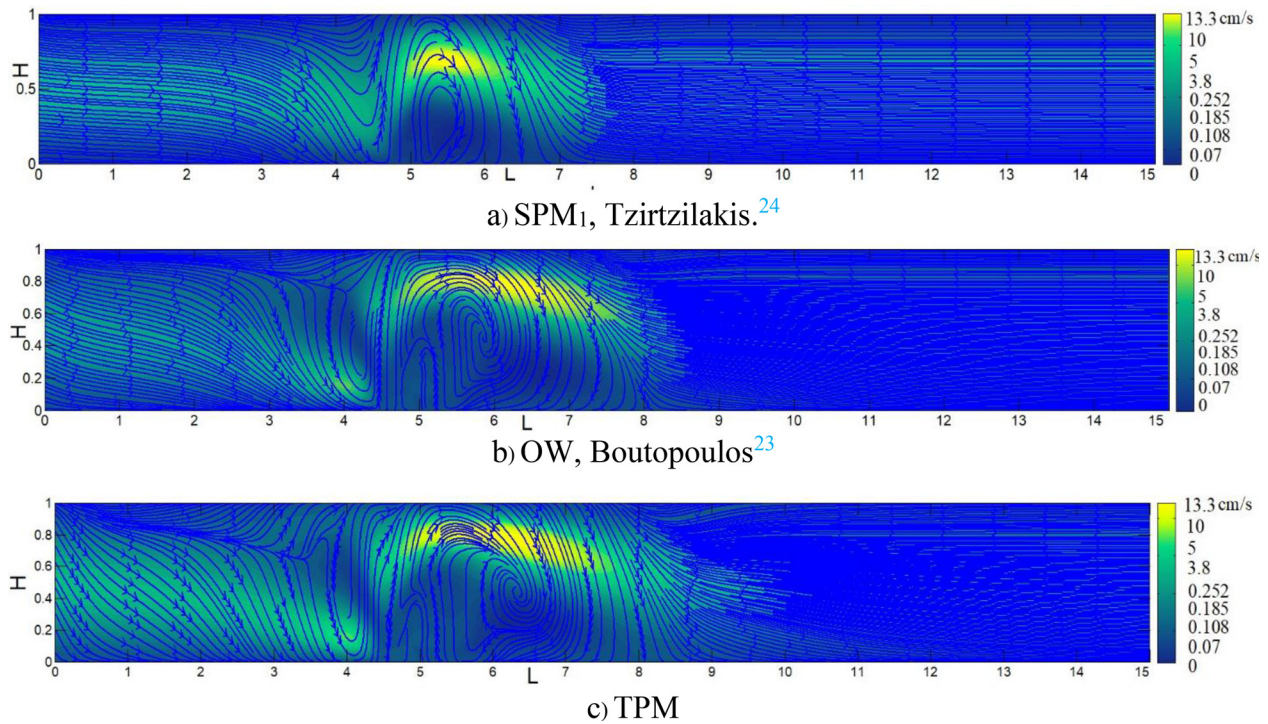


FIG. 3. Blood flow, case 2. The reference models vs TPM: $C_v = 0.001$ and $d = 250$. The curves show the stream lines. The density plot shows the magnitude of the velocity.

$$Nu = \frac{h_T(y)h_C}{k}, \tag{30}$$

where h_C is the diameter of the tube and h_T is the local heat transfer parameter given by

$$h_T = \frac{q_T}{T_w - T_m}. \tag{31}$$

$T_m(y)$ is the mean temperature of the fluid, $T_w(y)$ is the temperature of the wall, and q_T is the convective heat transfer. The flow of water

mixed with Al_2O_3 is characterized by $C_v = 0.04$, $q = 1000$, and $d = 250$. The results obtained by the SM₁, SM₂, OW, and the proposed TPM are compared with the above experiments in Table I. Note that Boutopoulos *et al.*²³ do not include the temperature equation. Hence, the temperature is simulated by the one-phase version of Eq. (3), where $\rho = 996 \text{ kg/m}^3$, and $c = 4180 \text{ J/kgK}$.

The average least squares error for SM₁ is 4.8%, for OW is 3.3%, and for SM₂ is 3.4%. The TPM shows the least squares error of about 5%. Therefore, the accuracy of the proposed TPM is comparable with

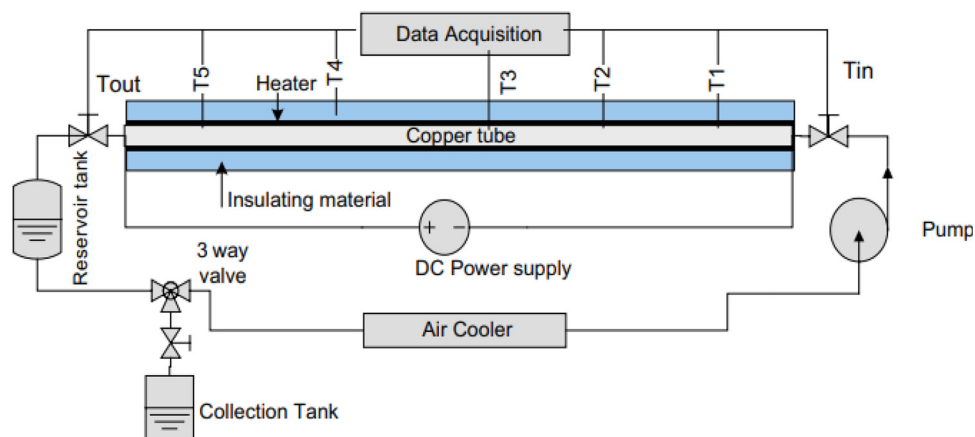


FIG. 4. Experimental setup of Wen and Ding.³⁵ Reproduced with permission from D. Wen and Y. Ding, "Experimental investigation into convective heat transfer of nanofluids at the entrance region under laminar flow conditions," *Int. J. Heat Mass Transfer* 47(24), 5181–5188 (2004). Copyright 2004 Elsevier.

TABLE I. The average Nusselt number. The proposed model, SPM₁, SPM₂, and OW vs the experiments conducted by Wen and Ding.³⁵

Re	Proposed TPM	SM ₁ ²⁴	OW ²³	SM ₂ ²⁵	Experiments ³⁵
250	5.75	4.89	4.99	6.88	5.80
270	7.8707	7.01	7.45	7.75	8
300	8.0682	7.66	7.88	7.85	8.13

the preceding models when the magnetic field is not applied or is weak. Our second test applies to the recent experimental data by Abadeh *et al.*³⁶ The experiment was carried out on the flow of water and Fe₃O₄ through a circular tube under the constant magnetic field. The setup is similar to Wen and Ding.³⁵ A straight circular copper tube (2700 mm) with 7.7 mm outer and 0.7 mm inner diameter had a thermal conductivity of 385 W/mK. Six wires were installed to produce a magnetic field of about 0.13 T. $C_v \in [0.005, 0.01]$, $d = 250$. The average Nu obtained by the reference models and the proposed TPM is compared with the experimental results by Abadeh *et al.*³⁶ in Table II.

The average least squares error for SM₁ is 12%, for OW is 8.3%, and for TPM is 5.7%. Therefore, the TPM shows better accuracy in the presence of the MF.

B. Numerical experiments and discussion

Following Nacev *et al.*,³⁴ a magnet is located at 5, 10, and 15 cm below the wall. The magnetic field(MF), characterized by $B = 0.5 T$ and $B = 1.0 T$, is applied to the blood flow mixed with Fe₃O₄. The MNs are characterized by $M \approx 100$ kA/m and diameters of 250 800, and 20 000 nm. The numerical simulations are performed for $h = 2.0$ cm and $L = 30$ cm. These are the typical diameter and the length of a large blood vessel of a human. The MNs and the blood enter the vessel at the left boundary. The left boundary condition for u is a parabola such that $\max(u) = u_{r1}$ at the centerline and $u = 0$ at the walls. The density of the MNs and the blood is $\rho = 1050$ kg/m³ and $\rho_p = 5200$ kg/m³, respectively. The dynamic viscosity of the blood is $\mu = 3.2 \times 10^{-3}$ kg/(m s). The Reynolds numbers and 3.1×10^{-3} for $d = 250$ and 800, respectively. The drag factor $f = 1$. When $d = 20000$, $Re_p \approx 1.0$ and $f = 1.1$. The thermal conductivity is $k = 2.2 \times 10^{-3}$ J/(m sK), and the heat capacity of the MNs and the blood is $c = 14.65$ J/kg K and $c_p = 670$ J/kg K, respectively. Hence, the Prandtl number is $Pr = \frac{c\mu}{k} \approx 21$. The parameters to control the transfer of the momentum and energy between the MNs and the blood are given by³⁷

$$\beta_1 = F_D \frac{h}{u_r} = \frac{18\mu}{d^2 \rho_p C_c} \frac{h}{u_r}, \quad \beta_2 = h_v \frac{h}{u_r} = \frac{6h_h}{d} \frac{h}{u_r}. \quad (32)$$

TABLE II. Average Nusselt number. Numerical models vs the experimental data of Abadeh *et al.*³⁶

Re	Proposed TPM	SM ₁ ²⁴	OW ²³	Experiments ³⁶
250	5.95	5.50	5.78	6.31
270	6.8707	6.05	6.30	6.99
300	8.0821	7.55	7.66	7.90

Therefore, $\beta_1 \propto \frac{1}{u_r}$, $\beta_2 \propto \frac{1}{u_r}$. The magnetic numbers characterize the blood and the MNs' flow under the impact of the MF,¹⁸

$$M_{nF} = \frac{MBh^2 \rho}{\mu^2 Re^2}, \quad M_{nF_p} = \frac{MBd^2 \rho^2}{\mu^2 \rho_p Re_p^2}, \quad (33)$$

$$M_{nM} = \frac{h^2 \sigma \mu_0^2 H_0^2}{\mu} \Rightarrow \frac{h^2 \sigma B_0^2}{\mu}, \quad M_{nM_p} = \frac{d^2 \sigma_p \mu_0^2 H_0^2}{\mu} \Rightarrow \frac{d^2 \sigma_p B^2}{\mu}. \quad (34)$$

Finally, $St = \frac{d^2 \rho_p C}{18\mu} \frac{u_r}{h}$. Hence, $St \propto d^2 u_r$. Substituting $u_r = \frac{Re\mu}{h\rho}$ yields $St \propto d^2 Re$.

C. Impact of the magnetic field (MF) in the case of combined magnetohydrodynamics (MHD) and ferrohydrodynamics (FHD)

In order to evaluate the impact of MF, consider $(a,b) = (10,10)$, $u_{r1} = 3.8$, $C_v = 0.004$, $d = 250$, $Re_p \approx 3.6 \times 10^{-2}$, $Re = 25$, and $St \approx 2.47 \times 10^{-4}$. Consider the following five cases:

Case 1: FHD: $B = 8$, $M_{nF} = 52500$, $M_{nF_p} \approx 265287$, $M_{nM} = 0$, $M_{nM_p} \approx 0$.

Case 2: MHD: $B = 2$, $M_{nF} = 0$, $M_{nF_p} \approx 0$, $M_{nM} = 4.0 \times 10^{-3}$, $M_{nM_p} \approx 1.42 \times 10^{-9}$.

Case 3: FHD/MHD: $B = 2$, $M_{nF} = 13125$, $M_{nF_p} \approx 165804$, $M_{nM} = 4.0 \times 10^{-3}$, $M_{nM_p} \approx 1.42 \times 10^{-9}$.

Case 4: FHD/MHD: $B = 5$, $M_{nF} = 32812$, $M_{nF_p} \approx 121$, $M_{nM} = 2.5 \times 10^{-2}$, $M_{nM_p} \approx 8.9 \times 10^{-9}$.

Case 5: FHD/MHD: $B = 8$, $M_{nF} = 52500$, $M_{nF_p} \approx 265287$, $M_{nM} = 6.4 \times 10^{-2}$, $M_{nM_p} \approx 2.2 \times 10^{-8}$.

Figures 5 and 6 depict the patterns of the blood and the MNs' flow. The steady-state time t_s is approximately 1.5 h for all cases with some decrease in time with the increase in the MF. For the same $B = 8$, let us compare case 1: FHD flow [Fig. 5(a)] and case 5: FHD/MHD flow [Fig. 5(e)]. Clearly, the Lorentz force (MHD) smooths the blood flow. Moreover, the vortex on the left side of the magnet in Fig. 5(a) practically disappears in Fig. 5(e). Furthermore, we analyze case 2 of the pure MHD flow for $B = 2$. Clearly, there is a disturbance near the magnetic source (Fig. 5b), but the entire flow pattern does not deviate significantly from the standard hydrodynamic flow.

Figures 5(c)–5(e) (cases: 3–5) show a combined FHD/MHD flow for $B = 2$, $B = 5$, and $B = 8$, respectively. Clearly, the pattern of the flow does not change significantly except some moderate smoothing by MHD. Note that when the gradient of the MF is strong the FHD effects are important, whereas MHD effects are strong when the MF gradient is low and $M_{nF_p} \approx 0$. Figure 6 shows the MNs flow for cases 1–5. The flow is affected in the same way that the blood flow is affected by FHD and MHD [Figs. 6(a)–6(e)]. However, the pattern of the MNs is different and does not follow the dynamics of the blood. Case 2 [Fig. 6(b)] of the pure MHD shows that the flow is not significantly affected although there are some minor disturbances. Since the size of the particles is small, the magnetic number M_{nM_p} is relatively low. The above-mentioned results presented in Figs. 5 and 6 comply with the analysis of the effects of MHD and FHD in Refs. 9, 10, and 18. As far as the clinical application is concerned, the evaluation of the impact of the irregularities of the flow on the patient and the balance among the possible negative effects of the vorticity and positive results of TMDD is an open problem. This requires further experimental research

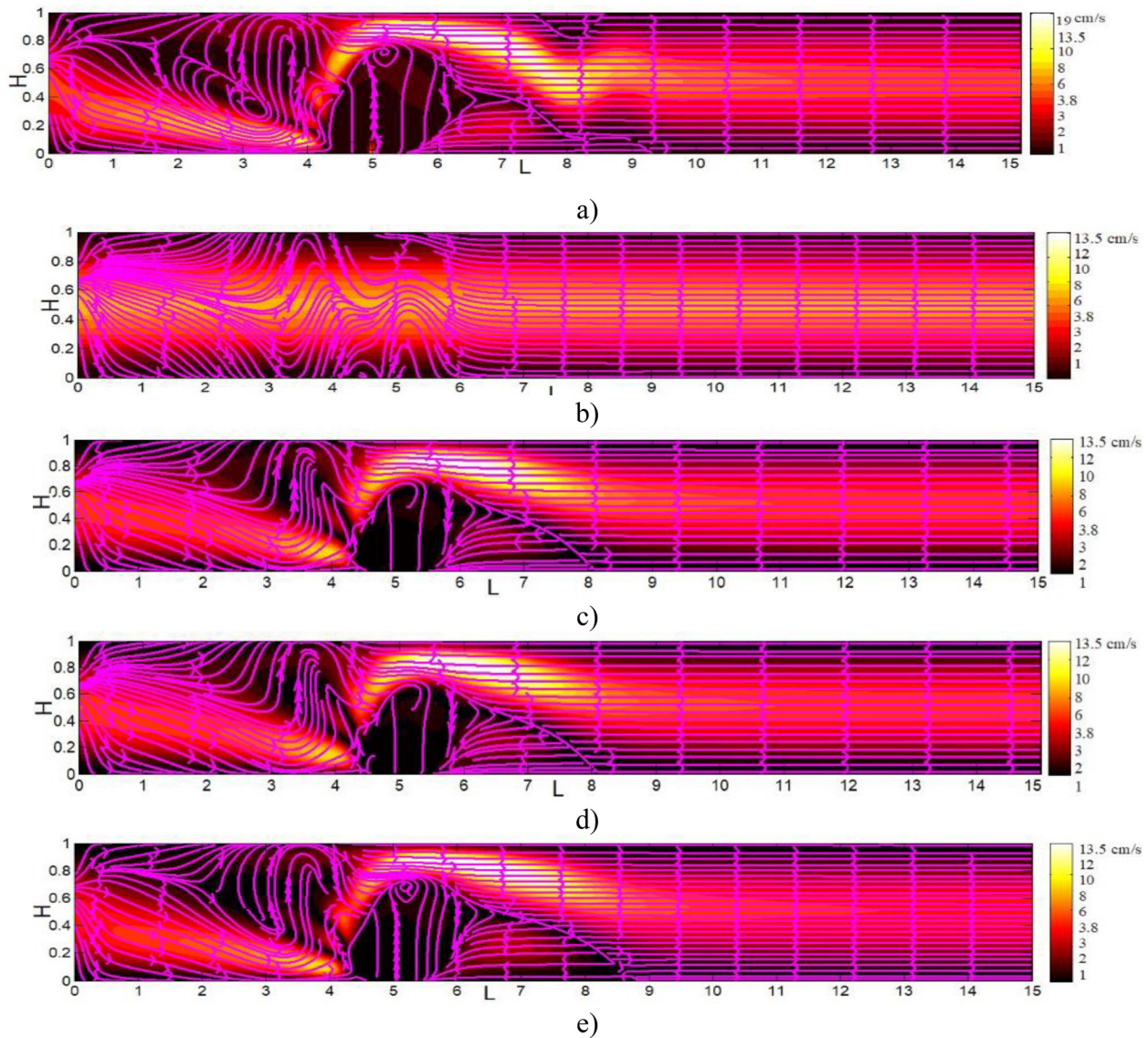


FIG. 5. Streamlines of the blood flow. The density plot shows the magnitude of the velocity: (a) case 1: FHD, (b) case 2: MHD, (c) case 3: FHD/MHD, $B = 2$, (d) case 4: FHD/MHD, $B = 5$, and (e) case 5: FHD/MHD $B = 8$.

outside the scope of this paper. However, the proposed model can be used as a second opinion to evaluate possible side effects.

D. Impact of the size of the magnetic nanoparticles (MNs) on the flow

The density of MNs ρ_p is defined by the density of the drug, the carrier, and the magnetic core. The model of ρ_p is represented by Eqs. (12a) and (12b). It includes the ratio of the magnetic core and the size of the MNs. It also includes a density of the shell, which is a mixture of a medical therapeutic drug and a carrier. The shell density is defined by proportion f_1 between the carrier and the drug ($0 \leq f_1 \leq 100\%$). Clearly, the same density of the MNs can be obtained for different

concentrations of the drug inside the MNs. Nevertheless, the density of the shell is approximately five times smaller than that of the MNs. Hence, the decrease in ρ_p for the same size of the MN may indicate the increase in the amount of the drug. On the other hand, we have to keep the magnetic core sufficiently large so that the MNs are attracted by the magnet.

Consider $(a,b) = (10, 10)$, $u_{r1} = 3.8$, $C_v = 0.004$, $B = 5$, $f = 1$, and $Re \approx 250$. The density of the MNs without the shell is $\rho_{core} = 5200$.

Consider the following four cases:

Case 1: $f_1 = 0$ $d = 250$, $St \approx 3.5 \times 10^{-4}$, $Re_p \approx 8.2 \times 10^{-4}$, $M_{nfp} \approx 98153$, $M_{nm_p} \approx 6.2 \times 10^{-9}$.

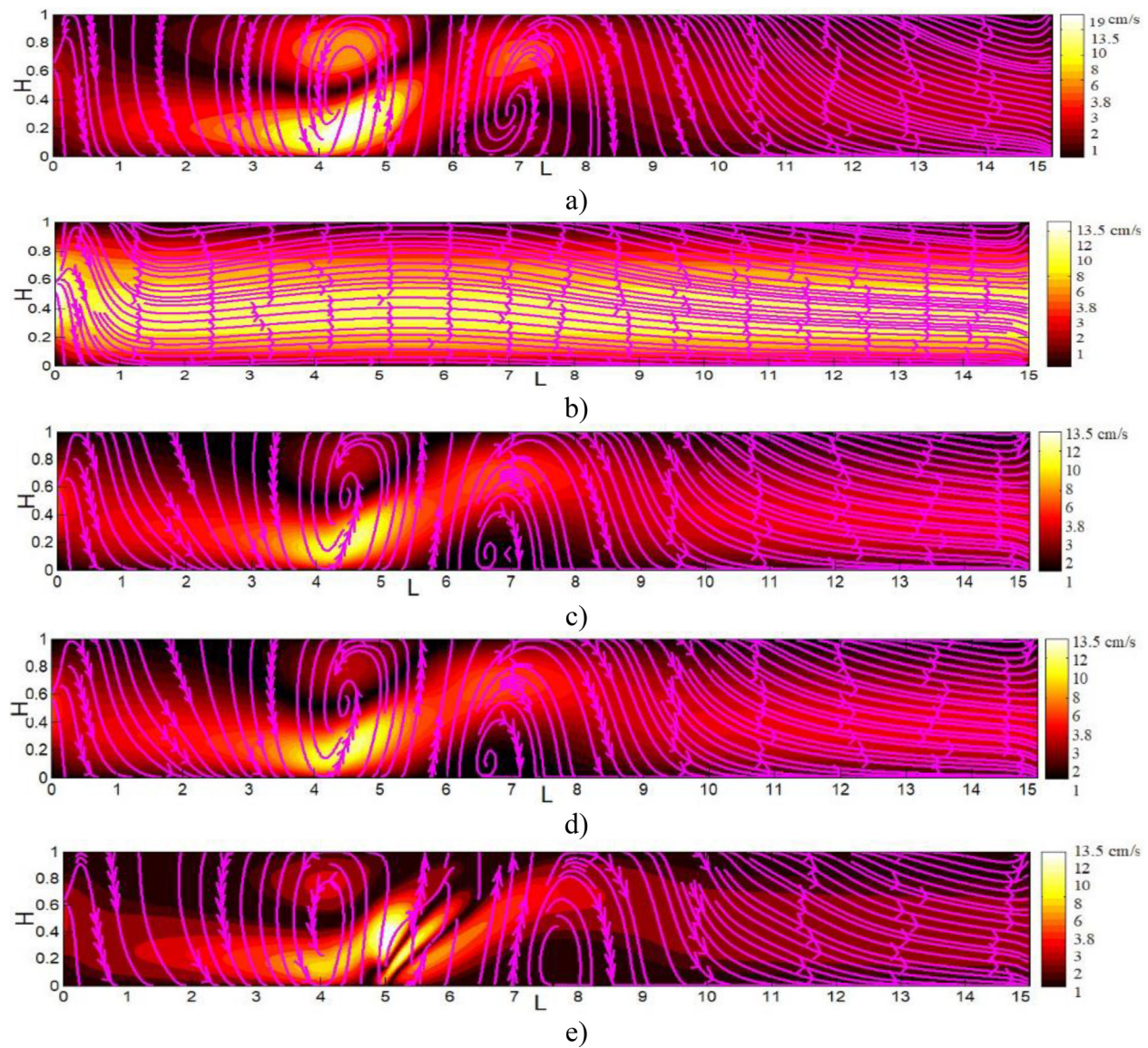


FIG. 6. Streamlines of the MNs' flow. The density plot shows the magnitude of the velocity: (a) case 1: FHD, (b) case 2: MHD, (c) case 3: FHD/MHD, $B=2$, (d) case 4: FHD/MHD, $B=5$, and (e) case 5: FHD/MHD, $B=8$.

Case 2: $f_1 = 30\%$ $d = 300$, $St \approx 2.47 \times 10^{-4}$, $Re_p \approx 9.8 \times 10^{-4}$, $M_{nFp} \approx 165804$, $M_{nMp} \approx 8.9 \times 10^{-9}$.

Case 3: $f_1 = 50\%$ $d = 500$, $St \approx 1.13 \times 10^{-4}$, $Re_p \approx 1.64 \times 10^{-3}$, $M_{nFp} \approx 602700$, $M_{nMp} \approx 2.4 \times 10^{-8}$.

Case 4: $f_1 = 50\%$ $d = 20,000$, $St \approx 1.23 \times 10^{-2}$, $Re_p \approx 6.5 \times 10^{-2}$, $M_{nFp} \approx 602700$, $M_{nMp} \approx 3.9 \times 10^{-5}$.

The magnetic numbers $M_{nF} \approx 32812$, $M_{nM} = 2.5 \times 10^{-2}$. The streamlines of the blood flow for cases 1–3 in Figs. 7(a)–7(c) correspond to the drug concentration of 0, 30, and 50%. The size of the MNs increases according to models (12a) and (12b). Figures 7(a)–7(c) show minor changes in the pattern of the blood flow. Circulation is characterized by the strong vortices and backflows.

The flow pattern for $f_1 = 0$ and 30% ($d=250$ and 300, respectively) practically does not change. When $f_1 = 50\%$ and $d = 500$, the structure of the lower vortex changes slightly. However, when $f_1 = 50\%$ and $d = 20,000$ [Fig. 7(e)], the pattern transforms. In particular, the flow at the upper boundary opposite the magnet generates a fully formed vortex, whereas the lower vortex increases. This is because of the substantial increase in the magnetic and Reynolds numbers, cf. case 3: $Re_p \approx 1.64 \times 10^{-3}$, $M_{nMp} \approx 2.4 \times 10^{-8}$ and case 4: $Re_p \approx 6.5 \times 10^{-2}$, $M_{nMp} \approx 3.9 \times 10^{-5}$. The MNs' flows in Figs. 8(a)–8(d) for cases 1–4, respectively, display patterns totally different from those of the blood flow in Fig. 7. However, the effect of the combination of the size/ density of the MNs works along the

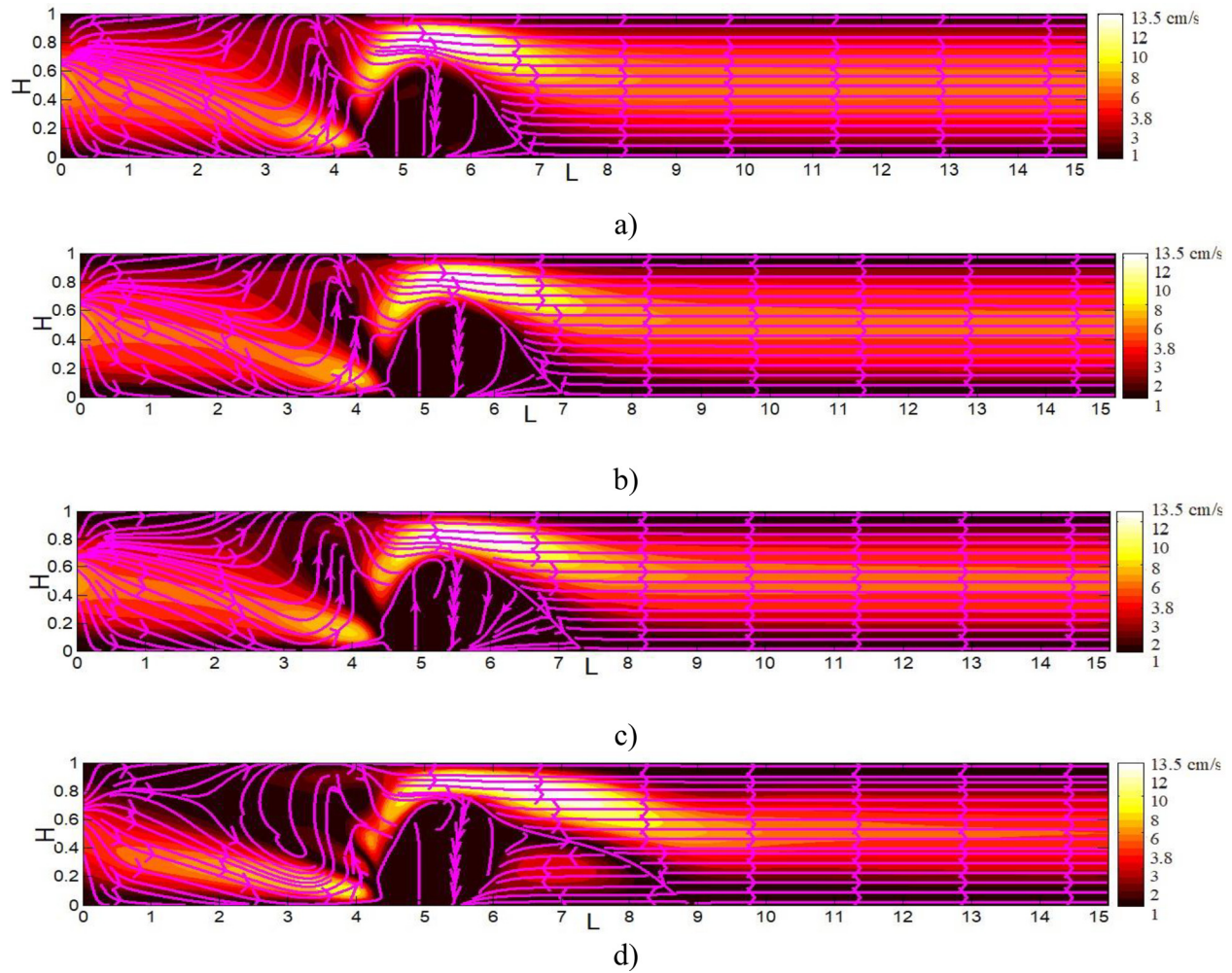


FIG. 7. Streamlines of the blood for different size and density of the MNs. The density plot shows the magnitude of the velocity: (a) $d = 250$, $f_1 = 0$, (b) $d = 300$, $f_1 = 30\%$, (c) $d = 500$, $f_1 = 50\%$, and (d) $d = 20\,000$, $f_1 = 50\%$.

same lines. The flow patterns shown in Figs. 8(a)–8(c) corresponding to cases 1–3 are approximately the same, whereas case 4 depicted in Fig. 8(d) shows the formation of a new vortex. Interestingly enough, the new vortex has a totally different location and shape as compared to the newly formed vortex of the blood flow in Fig. 7(d).

E. Impact of the size of the magnetic nanoparticles (MNs) on the temperature

Consider $Re = 25$, $B = 0.5$, and $C_v = 0.04$. The initial temperature is $T(x, y, 0) = 37^\circ\text{C}$. The boundary conditions are $T(x, y, t)|_{\text{left boundary}} = 37^\circ\text{C}$ and $\frac{\partial T}{\partial n}|_{\text{other boundaries}} = 0$.

Furthermore, $Re_p \approx 0.01$, $Re = 250$, $u_r = u_{r1} = 3.8$, $Pr = 25$, $Ec = 4.2 \times 10^{-5}$, $M_{nF} = 3281$, and $M_{nF_p} \approx 6677$. The thermal conductivity of blood increases with an increase in the size of the MNs. Recall that the exchange of the energy between the blood and the MNs

is proportional to parameter β_2 [Eqs. (28a)–(29a)]. This parameter is evaluated by Gireesha *et al.*³⁷ as follows:

$$\beta_2 = \frac{6k}{d^2} \left(2.0 + 0.6Re_p^{1/2}Pr^{1/3} \right) \frac{h}{u_r}. \quad (35)$$

Hence, the exchange is proportional to $1/d^2$. The impact of the size of the MNs on the temperature profile is illustrated in Figs. 9 and 10. Due to the magnetocaloric effect and the energy exchange defined by Eq. (35), the temperature rises in the region of the strong MF. The maximum increase in temperature inside the lower vortex is 2.1°C (from 37 to 39.1°C). The case of $\beta_2 = 0$ in Fig. 9(a) (magnetocaloric effect) complies with the results of Tzirtzilakis.²⁴ For $d = 250$, the temperature starts increasing in the MF region at $t \approx 13\text{min}$ and reaches approximately 39.1°C at the steady state, $t \approx 1.5\text{h}$. When $d = 800$, the temperature reaches a maximum of about 39.1°C at $t \approx 1.2\text{h}$, whereas $d = 20\,000$ requires only about 0.52h . The maximum temperature of the MNs reaches approximately 38.8°C with negligible

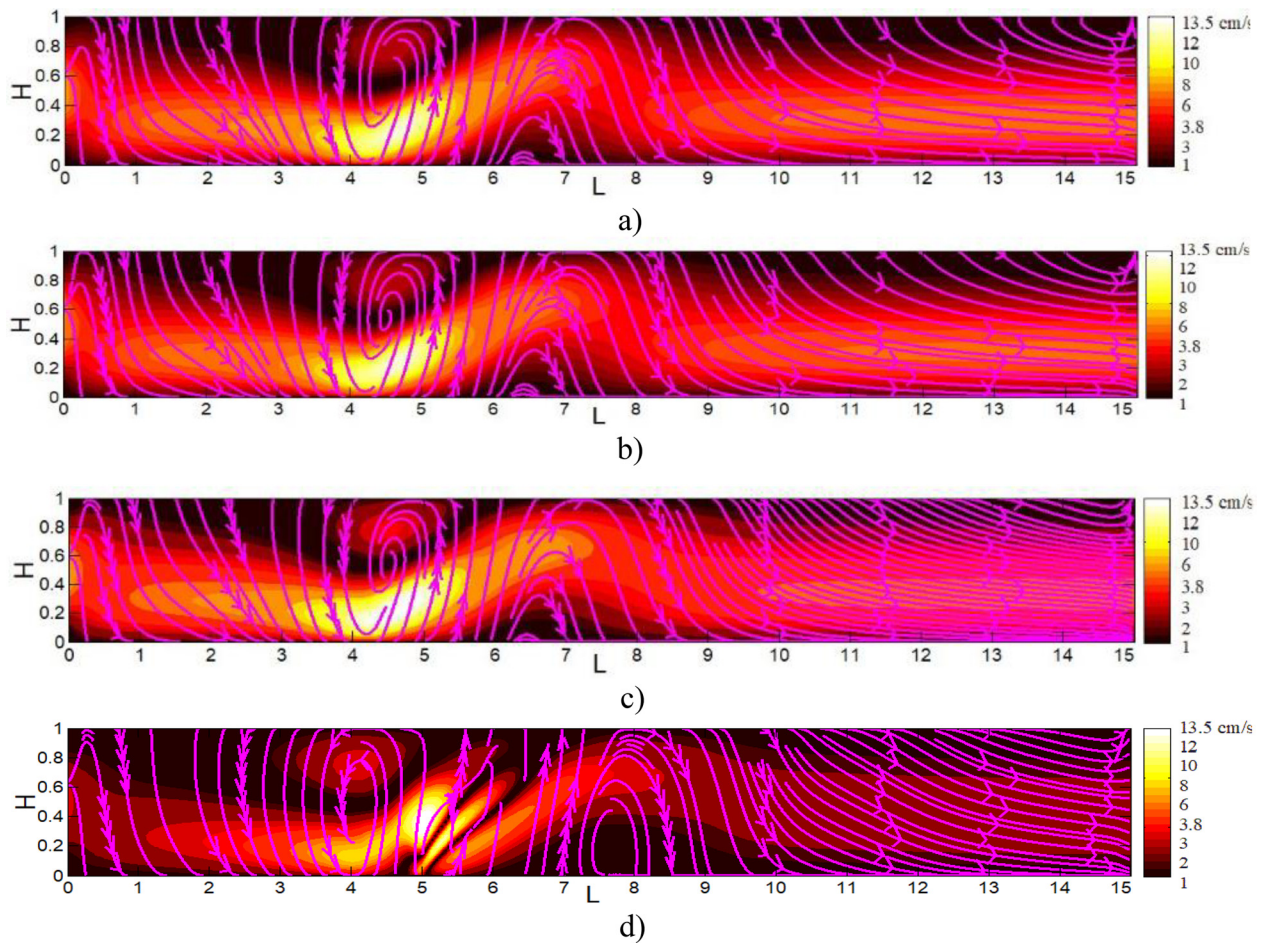


FIG. 8. Streamlines for different sizes of MNs. The density plot shows the magnitude of the velocity: (a) $d = 250$, $f_1 = 0$, (b) $d = 300$, $f_1 = 30\%$, (c) $d = 500$, $f_1 = 50\%$, and (d) $d = 20\,000$, $f_1 = 50\%$.

differences in the second digit after the decimal point for different sizes of the MNs (Fig. 10). Such a temperature increase may have a negative impact on long-term treatments such as chemotherapy. As an example, we refer to the effects of the MRI with the MF of about 4T as noticed in Refs. 38 and 39. The patients reported sensations of nausea, vertigo, metallic taste, or sleepiness after the treatments.

VI. CONCLUSIONS

The proposed two-phase two-way coupled model makes it possible to simulate the dynamics of magnetic nanoparticles (MNs) in the blood flow under the impact of the strong magnetic field (MF). The most important feature of the model is the inverse impact of the MNs on the blood flow.

The model shows that the Lorentz force (magnetohydrodynamics) may smooth the blood flow by slightly reducing the vortices created by FHD (ferrohydrodynamics). The pure flow of the MNs is close to the classic hydrodynamic flow with some minor disturbances. The relationship between the magnetic core and the shell consisting of the mixture of the therapeutic drug and the carrier makes it possible to

evaluate the required size and the density of the MNs. This relationship also requires to setup the concentration of the drug $0 \leq f_1 \leq 100\%$ in the shell. Increasing the size of the MNs enhances the TMDD zone. For instance, the scenarios $f_1 = 50\%$, $d = 500$ vs $f_1 = 50\%$, $d = 20\,000$ show a considerable difference in the patterns of the blood and the MNs. However, a strong MF combined with large particles may clog up the blood vessels while a weak MF and small MNs may not be able to deliver the drug.

The proposed two-way coupled energy equations make it possible to analyze the impact of the size of the MNs on the temperature of the blood flow. The model shows that under certain conditions, the large MNs induce a temperature increase of about 2°C over a relatively large region. Such an increase combined with the increased vorticity may lead to a negative impact on the patient.

The model has a number of limitations. The magnet is represented as a pointwise wire. However, the shape of the magnet can vary. The corresponding MF depends on the shape and the orientation of the magnet. This effect has not been fully considered. The dependence of the heat transfer on the MF has not been considered either.

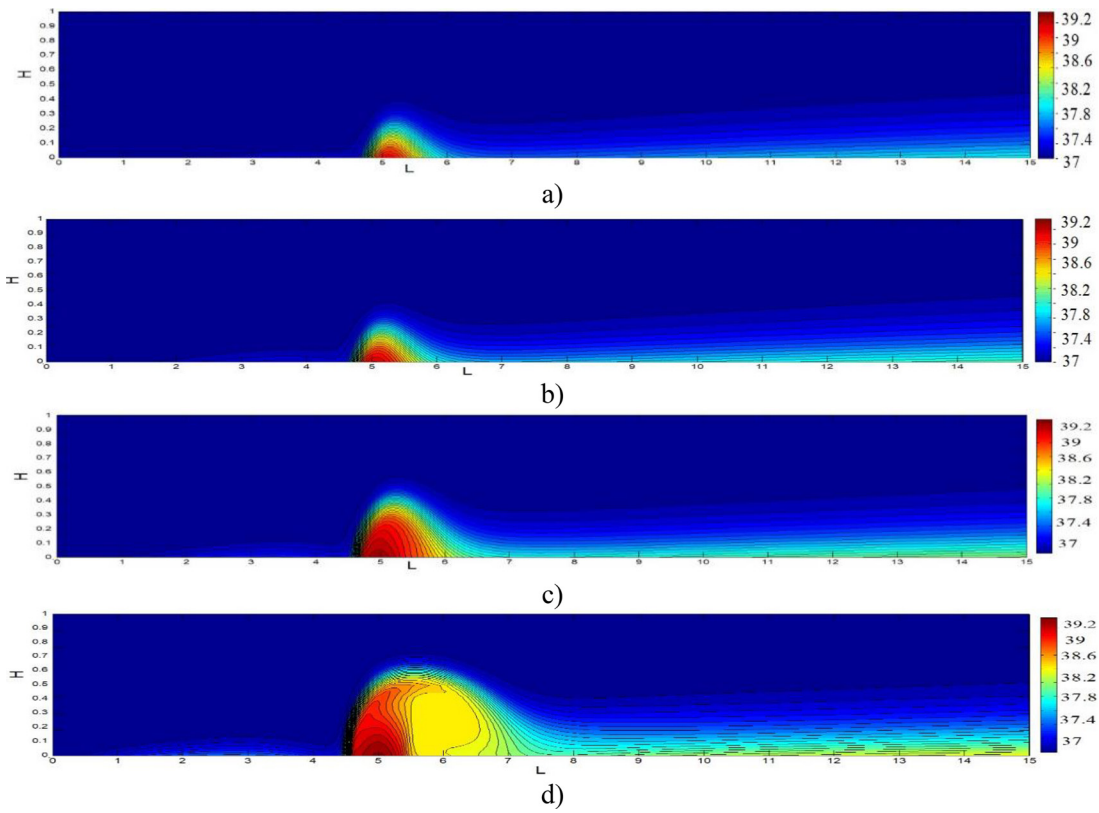


FIG. 9. Temperature of the blood flow: (a) $\beta_2 = 0$, (b) $d = 250$, (c) $d = 800$, and (d) $d = 20\,000$.

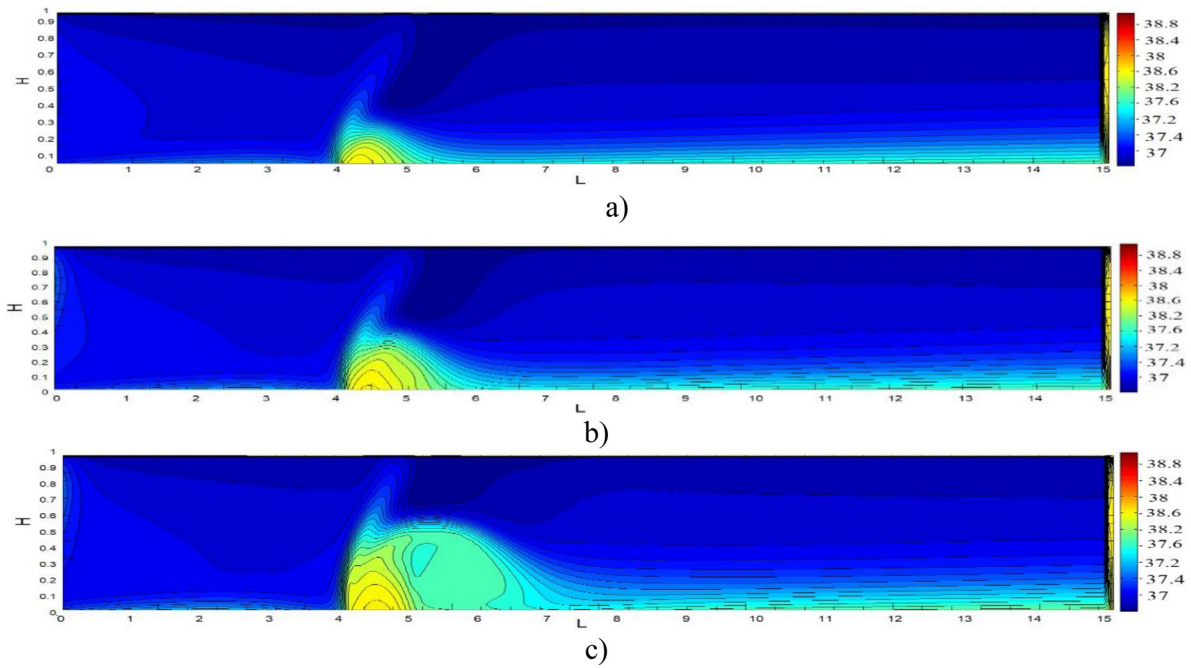


FIG. 10. Temperature of the MNs' flow: (a) $d = 250$, (b) $d = 800$, and (c) $d = 20\,000$.

The model does not include a number of important effects such as the Brownian motion of the nanoparticles, the acoustic radiation force, the lift force (Saffman and Magnus effects), and the thermophoretic force. Finally, the shape of the MNs (an important factor) has not been included in the proposed two-phase equations. Therefore, future research includes further validation of the model using new experimental results and modifying the model to include the above-mentioned effects.

ACKNOWLEDGMENTS

This research was supported by the Center of Excellence in Biomedical Engineering, Thammasat University, Thailand. We wish to thank the Referees for their insightful comments and critique.

AUTHOR DECLARATIONS

Conflict of Interest

The authors declare that there is no conflict of interest.

DATA AVAILABILITY

The data that support the findings of this study are available within the article.

NOMENCLATURE

a	x -coordinate of the magnet, cm
b	y -coordinate of the magnet, cm
B	Magnetic field strength, T
c	Heat capacity of the blood, J/kg K
c_p	Heat capacity of the MNs, J/kg K
f_1	Fractional loading of the magnetic therapeutic drug, %
h	Vessel height, cm
H	Magnetic flux density, kA/m
h_c	Diameter of the tube, cm
J	Vorticity function, 1/s
k	Thermal conductivity of the blood, J/ms K
L	Vessel length, cm
M	Magnetization, kA/m
q	Heat flux, W/m ²
T	Temperature of the blood, °C
T_c	The Curie temperature, °C
T_c	Cunningham correction coefficient, dimensionless
T_p	Temperature of the MNs, °C
T_w	Temperature of the walls, °C
t_C	Time of the beginning of circulation, h
t_S	Steady state time, h
u	Horizontal component of the velocity of the blood, cm/s
u_p	Horizontal component of the velocity of the MNs, cm/s
u_r	Maximum horizontal entrance velocity of the blood, cm/s
u_{r1}	Maximum horizontal entrance velocity of the MNs, cm/s
$\mathbf{V} = (u, v)$	Velocity vector of the blood, cm/s

$\mathbf{V}_p = (u_p, v_p)$	Velocity vector of the MNs, cm/s
v	Vertical component of the velocity of the blood, cm/s
v_p	Vertical component of the velocity of the MNs, cm/s
λ_a	Average free path of the magnetic nanoparticle, μm
μ	Dynamic viscosity of the blood, kg/m s
ρ	Density of the blood, kg/m ³
ρ_p	Density of the MNs, kg/m ³
ρ_{drug}	Density of the drug, kg/m ³
$\rho_{carrier}$	Density of the carrier, kg/m ³
σ	Thermal conductivity of the blood, S/m
σ_p	Thermal conductivity of the MNs, S/m
ψ	Stream function, m ² /s

Acronyms Terms

BFD	Biofluid dynamics
FHD	Ferrohydrodynamics
MHD	Magneto hydrodynamics
MF	Magnetic field
MNs	Magnetic nanoparticles
TMDD	Targeted magnetic drug delivery

REFERENCES

- 1E. Karvelas, C. Liosis, A. Theodorakakos, I. Sarris, and T. Karakasidis, "An optimized method for 3D magnetic navigation of nanoparticles inside human arteries," *Fluids Barriers CNS* **6**, 97 (2021).
- 2S. Mukherjee, L. Liang, and O. Veisheh, "Recent advancements of magnetic nanomaterials in cancer therapy," *Pharmaceutics* **12**, 147 (2020).
- 3M. P. Bui, T.-A. Le, and J. Yoon, "A magnetic particle imaging-based navigation platform for magnetic nanoparticles using interactive manipulation of a virtual field free point to ensure targeted drug delivery," *IEEE Trans. Ind. Electron.* **68**, 12493–12503 (2021).
- 4I. Sur and J. Taipale, "The role of enhancers in cancer," *Nat. Rev. Cancer* **16**, 483–493 (2016).
- 5S. Kenjereš and J. L. Tjin, "Numerical simulations of targeted delivery of magnetic drug aerosols in the human upper and central respiratory system: A validation study," *R. Soc. Open Sci.* **4**, 170873 (2017).
- 6K. J. Widder, R. M. Morris, G. Poore, D. P. Howard, and A. E. Seneyi, "Tumor remission in Yoshida sarcoma-bearing rats by selective targeting of magnetic albumin microspheres containing doxorubicin," *Proc. Natl. Acad. Sci. U. S. A.* **78**, 579–581 (1981).
- 7O. Friman *et al.*, "Probabilistic 4D blood flow tracking and uncertainty estimation," *Med. Image Anal.* **15**, 720–728 (2011).
- 8V. Martin, A. Drochon, O. Fokapu, and J.-F. Gerbeau, "Magneto hemodynamics in the aorta and electrocardiograms," *Phys. Med. Biol.* **57**, 3177–3195 (2012).
- 9M. A. Xenos and E. E. Tzirtzilakis, "MHD effects on blood flow in a stenosis," *Adv. Dyn. Syst.* **8**, 427–437 (2013).
- 10A. Raptis, M. Xenos, E. Tzirtzilakis, and M. Matsagkas, "Finite element analysis of magneto hydrodynamic effects on blood flow in an aneurysmal geometry," *Phys. Fluids* **26**, 101901 (2014).
- 11S. Goudarzi, S. Yekani Motlagh, and H. Soltanipour, "Two-phase simulation of MHD and FHD impacts on the natural convection of a magnetic nanofluid within a porous cavity," *Proc. Inst. Mech. Eng., Part D* **6**, 9–9 (2022).
- 12M. Sakthivel and K. Anupindi, "An off-lattice Boltzmann method for blood flow simulation through a model of irregular arterial stenosis: The effects of amplitude and frequency of the irregularity," *Phys. Fluids* **33**, 031912 (2021).

- ¹³Y. Chen, X. Zhang, L. Ren, Y. Geng, and G. Bai, "Analysis of blood flow characteristics in fractal vascular network based on the time fractional order," *Phys. Fluids* **33**, 041902 (2021).
- ¹⁴L. Zhu and K. Sakai, "Simulation of blood flow past distal arteriovenous-graft anastomosis with intimal hyperplasia," *Phys. Fluids* **33**, 051905 (2021).
- ¹⁵A. K. Roy and S. Shaw, "Shear augmented microvascular solute transport with a two-phase model: Application in nanoparticle assisted drug delivery," *Phys. Fluids* **33**, 031904 (2021).
- ¹⁶V. C. Loukopoulos and E. E. Tzirtzilakis, "Biomagnetic channel flow in a spatially varying magnetic field," *Int. J. Eng. Sci.* **42**, 571–590 (2004).
- ¹⁷E. E. Tzirtzilakis and V. C. Loukopoulos, "Biofluid flow in a channel under the action of a uniform localized magnetic field," *Comput. Mech.* **36**, 360–374 (2005).
- ¹⁸E. E. Tzirtzilakis, "A mathematical model for blood flow in magnetic field," *Phys. Fluids* **17**, 077103 (2005).
- ¹⁹S. Kenjeres, "Numerical analysis of blood flow in realistic arteries subjected to strong non-uniform magnetic fields," *Int. J. Heat Fluid Flow* **29**, 752–764 (2008).
- ²⁰A. Alshare and B. Tashtoush, "Simulations of magneto-hemodynamics in stenosed arteries in diabetic or anemic models," *Comput. Math. Methods Med.* **2016**, 8123930.
- ²¹S. Bose and M. Banerjee, "Magnetic particle capture for biomagnetic fluid flow in stenosed aortic bifurcation considering particle–fluid coupling," *J. Magn. Magn. Mater.* **385**, 32–46 (2015).
- ²²A. Sharifi, S. Y. Motlagh, and H. Badfar, "Numerical investigation of magnetic drug targeting using magnetic nanoparticles to the aneurysmal vessel," *J. Magn. Magn. Mater.* **474**, 236–245 (2019).
- ²³I. D. Boutopoulos, D. S. Lampropoulos, G. C. Bourantas, K. Miller, and V. C. Loukopoulos, "Two-phase biofluid flow model for magnetic drug targeting," *Symmetry* **12**, 1083 (2020).
- ²⁴E. E. Tzirtzilakis, "A simple numerical methodology for BFD problems using stream function vorticity formulation," *Commun. Numer. Methods Eng.* **24**, 683–700 (2007).
- ²⁵V. Bianco, F. Chiacchio, O. Manca, and S. Nardini, "Numerical investigation of nanofluids forced convection in circular tubes," *Appl. Therm. Eng.* **29**, 3632–3642 (2009).
- ²⁶M. Sheikholeslami, M. M. Rashidi, and D. D. Ganji, "Effect of non-uniform magnetic field on forced convection heat transfer of Fe₃O₄-water nanofluid," *Comput. Methods Appl. Mech. Eng.* **294**, 299–312 (2015).
- ²⁷A. A. Minea, "A review on electrical conductivity of nanoparticle-enhanced fluids," *Nanomaterials* **9**, 1592 (2019).
- ²⁸J. Rosen, *Encyclopedia of Physics (Facts on File Science Library)* (Facts on File, New York, 2004).
- ²⁹E. E. Tzirtzilakis, "Biomagnetic fluid flow in an aneurysm using ferrohydrodynamics principles," *Phys. Fluids* **27**, 061902 (2015).
- ³⁰H. Matsuki, K. Yamasawa, and K. Murakami, "Experimental considerations on a new automatic cooling device using temperature-sensitive magnetic fluid," *IEEE Trans. Magn.* **13**, 1143–1145 (1977).
- ³¹W. E. Ranz and W. R. Marshall, "Evaporation from drops, Part I," *Chem. Eng. Prog.* **48**(3), 141–146 (1952).
- ³²M. Cervera, R. Codina, and M. Galindo, "On the computational efficiency and implementation of block-iterative algorithms for nonlinear coupled problems," *Eng. Comput.* **13**, 4–30 (1996).
- ³³Á. L. D. Bortoli, Á. L. De Bortoli, G. S. L. Andreis, and F. N. Pereira, "Numerical methods for reactive flows," *Modeling and Simulation of Reactive Flows* (Elsevier, 2015), pp. 123–169.
- ³⁴A. Nacev, C. Beni, O. Bruno, and B. Shapiro, "The behaviors of ferro-magnetic nano-particles in and around blood vessels under applied magnetic fields," *J. Magn. Magn. Mater.* **323**, 651–668 (2011).
- ³⁵D. Wen and Y. Ding, "Experimental investigation into convective heat transfer of nanofluids at the entrance region under laminar flow conditions," *Int. J. Heat Mass Transfer* **47**(24), 5181–5188 (2004).
- ³⁶A. Abadeh *et al.*, "Experimental characterization of magnetic field effects on heat transfer coefficient and pressure drop for a ferrofluid flow in a circular tube," *J. Mol. Liq.* **299**, 112206 (2020).
- ³⁷B. J. Gireesha, P. Venkatesh, N. S. Shashikumar, and B. C. Prasannakumara, "Boundary layer flow of dusty fluid over a radiating stretching surface embedded in a thermally stratified porous medium in the presence of uniform heat source," *Nonlinear Eng.* **6**, 31–41 (2017).
- ³⁸J. F. Schenck *et al.*, "Human exposure to 4.0-Tesla magnetic fields in a whole-body scanner," *Med. Phys.* **19**, 1089–1098 (1992).
- ³⁹T. Yamamoto, Y. Nagayama, and M. Tamura, "A blood-oxygenation-dependent increase in blood viscosity due to a static magnetic field," *Phys. Med. Biol.* **49**, 3267–3277 (2004).